Thermocline entrainment in stratified energy stores

THERMOCLINE ENTRAINMENT IN STRATIFIED ENERGY STORES

J. van Berkel, A. A. van Steenhoven and C.C.M. Rindt
Eindhoven University of Technology,
Faculty of Mechanical Engineering, WOC/WET
PO-box 513, 5600 MB Eindhoven, The Netherlands

Abstract—Thermocline-entrainment as encountered in stratified stores is investigated numerically and experimentally in an adiabatic box containing a quasi-stationary thermocline. Experiments and finite volume simulations are shown to agree well and give complementary insights. It appears that at the point of collision of the jet with the thermocline, shear layers develop which are unstable resulting in secondary Kelvin-Helmholtz- and tertiary Görtler waves. Along with the shear layers, thermocline fluid is dragged into the mixed layer by virtue of viscous forces.

1. INTRODUCTION

Notwithstanding the present-day application of thermally stratified energy storage little is known about the mixing phenomena that occur in such storage. This especially applies to situations in which stratification is weak and easily distorted by inflow inertia forces : short cycle times, low temperatures and small temperature differences. The goal of the present research is to provide a more fundamental basis for the current empirically based design guide lines. Considered are two layer water stores in their simplest form : a hexahedron equipped with top and bottom linear slot in- and outlet diffusers. Following the common operation strategy of stratified stores, involving elimination of strongly varying outlet temperatures by preservation of the steep temperature gradient zone (the thermocline) inside the storage, the thermocline is studied in its quasi-stationary mode. In this thermocline preservation mode two important phenomena affect the storage performance negatively, being 1) thermocline erosion (mixing of thermal energy) and 2) ineffective usage of storage volume as a result of the finite height of the thermocline.
Research (Hussain & Wildin, 1991) has shown that the flow pattern in a two layer stratified store features a non-buoyant free- or wall jet, caused by the storage inflow, colliding with the thermocline.

For easy observation and analysis of the entrainment process, the two layer thermally stratified storage has been abstracted to a conceptual, numerical and material model, in which the thermocline advances due to entrainment only.

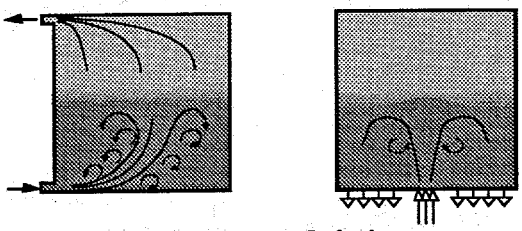

Figure 1 Large scale flow patterns. Left the storage and right its abstraction.

By injecting and withdrawing fluid in one layer at exactly the same rate the thermocline is arrested and as a result it attains a steady state. As a spin-off this configuration also applies to related topics like jet mixing in chemical reactors and jet ventilation in oil tanks, lakes or rooms. In a previous paper (Van Berkel, 1995) experimental and numerical results on the overall flow pattern and entrainment rate have been discussed. This paper concerns the physics of the entrainment mechanism itself.

2. NUMERICAL AND EXPERIMENTAL METHODS USED

The thermocline entrainment process is simulated using a finite difference/volume method using an equidistant square mesh for the momentum equation (with staggered orientation of pressure and velocity point) and the energy equation. The code which for a large part comprises the Marker-And-Cell (MAC)-formulation developed by Harlow and Welch (1965) is an adapted version of the code originally written by Nieuwstadt and modified by Bastiaans (Bastiaans, 1994). The code has been selected for its simplicity, accuracy and computational efficiency both in 2- as well as in 3D. The lack of geometrical flexibility, posed by the Cartesian spatial discretization, is not felt as a very serious drawback since the thermocline/jet collision process under consideration is assumed to be marginally affected by boundary geometry.
In essence the method is a pressure-correction method, projecting an intermediate velocity field $\mathbf{u}^*$ obtained from the Navier-Stokes equation (excluding pressure), to a divergence free velocity field $\mathbf{u}^{n+1}$ by evaluating the pressure gradient term in the separate correction step. In this correction step, the Poisson equation for pressure is solved directly using a five–point finite difference approximation on a staggered grid (Schumann &

Sweet, 1976). Time stepping is done using the central second order accurate Leap-Frog scheme with weakly coupled odd and even time levels. The instationary energy equation is evaluated in a separate step. To reduce artificial diffusion, which would render the numerical simulation highly inaccurate, advection of momentum and thermal energy are discretized using second order accurate central (momentum) or upwind (temperature) difference schemes. Common assumptions are made for the solution process : Boussinesq approximation, no viscous dissipation, no radiative heat transfer.

Boundary conditions are implemented using a shell of virtual cells enclosing the flow domain. The temperature boundary conditions are 1) set to T=20 °C at the inlet, 2) adiabatic at the walls and 3) advective ($\partial T/\partial t = -v_\perp \partial T/\partial n$) at the outlets. The kinematic boundary conditions are no slip everywhere and $v_\perp = 0$, v_{in} or v_{out} at the walls, inlet and outlets respectively. For pressure everywhere $\partial P/\partial n = 0$ is set. The initial conditions are T = 40 °C and 20 °C for the upper- and lower layer respectively.

In the 2D-simulations presented here the flow domain consists of 178 x 160 cells, each cell having dimensions of 2.5 x 2.5 mm^2, which is smaller than the observed characteristic fluid motion length scale. Given the spatial resolution, the inlet slot is represented by 6 adjacent cells and the outlet by 8 equidistantly spaced pairs of cells on either side of the slot. Figure 2 shows the set-up used for the experimental investigation.

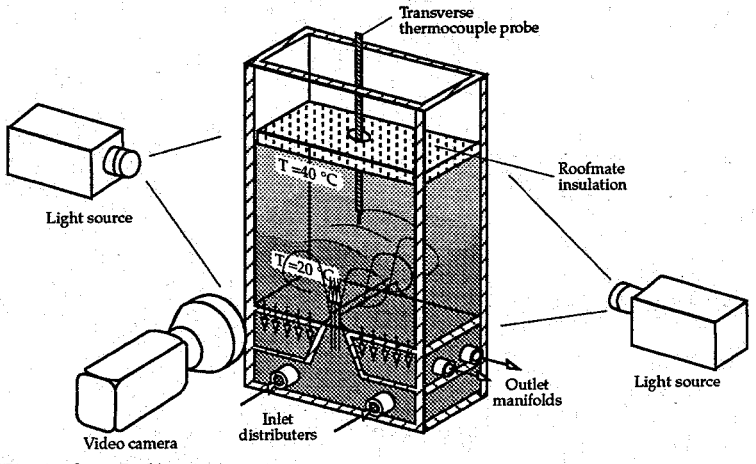

Figure 2 Laboratory set-up.

The domain of interest is sized 44.5 cm width x 40.0 cm height x 24 cm depth. The centrally placed, well rounded slot has a width of 1.5 cm. Withdrawal takes place through 8 x 12 uniformly distributed, 1 mm diameter holes on either sides of the slot. Flow stabilisation chambers ensure uniform withdrawal and injection. Water is circulated through the tank and a flow measurement device by a variable speed centrifugal pump. Two layer stratification is attained by means of an immersed electrical heater, heating up the top layer only to temperature of 40 °C. The lower layer has a temperature equal to the ambient temperature of 20 °C. During testing an insulation plate floating on top of the free surface prevents excessive heat loss. The centreline temperature profile is recorded using a vertical, linearly traversing ø 0.5 mm type K thermocouple probe.
Initially flow visualisation was done by the shadow graph technique and potassium-permanganate dye colouring. In that set-up the tank was illuminated from the backside, projecting an image on mat paper attached to the front side. Though easy to apply, the shadow graph technique shows fluid motions cumulative over the tank depth, making the results hard to interpret. In the present study flow visualisation is done by means of fluorescent dye being added to the top layer. A 1 - $1^1/_2$ cm thick vertical light sheet is created by illuminating the tank from both sides through slotted masks (not shown in figure 2), attached to the side walls, thereby creating a two-dimensional front view image.
Quantitative information concerning the flow field is obtained by Particle Tracking Velocimetry (PTV), using the version 2.0 Dig*Image* package developed by Dalziel (Dalziel, 1995). The 65 l tank content is seeded with 1.0 gr (whole field) or 2.0 gr (detail) *OptImage* particles having a nominal diameter of 250 μm. After recording of an experiment on tape, particles are tracked from tape at a frequency of 25 Hz. Sequentially 0.16 s averaged (4 samples) unstructured velocity field files are produced, incorporating the condition that a specific particle is recognised in all four frames. Finally the kinematics are derived by re-sampling the unstructured velocity data on a structured 60 x 45 grid using spline interpolation.
Measurements are taken in the front view plane (whole field and zoomed in on the shear layer), as well as in two vertical planes perpendicular to the front plate to obtain quantitative information on the velocities in the third dimension.

3. RESULTS

Experiments and simulations are done for several cases, designated by their overall Richardson- and Reynolds inlet numbers :

$$Ri_o = \frac{g' h}{u_{in}^2} \qquad Re_i = \frac{u_{in} b}{\nu} \tag{1}$$

In which g' is the apparent acceleration of gravity $g\ \Delta\rho/\rho$, h the distance of the thermocline from the jet origin ,u_{in} the jet inlet velocity, b the jet slot width and ν the kinematic viscosity. All experiments are performed for an inlet Reynolds number of 400. Here only the Ri_o=20 case will be considered of which figure 3 shows a fluorescent dye image.

Figure 3 Fluorescent dye image at Ri_o = 19.2, Re_i = 400.

Figure 3 shows a globally symmetric submerged fountain, colliding on the thermocline. In the mushroom shaped collision area the thermocline is smooth and sharp whereas it becomes wavy and diffuse on the edges. Frequently Kelvin-Helmholtz waves are observed on the shear layer between the colliding jet and ambient fluid. After formation of the KH-waves and occasional pairing, the shear layer is advected into the lower layer where chaotic mixing takes place.
Just vaguely seen is the meandering flow pattern of the jet. Close observation of the video recordings reveal that the shear layer instability is triggered by the swaying motion of the jet. The typical frequency of the jet meandering correspond with the Kelvin-Helmholtz frequency and amounts to $^1/_3$ - $^1/_2$ Hz. Typical wave length of the shear layer instability is 5 cm, whereas the jet buckling wave length is estimated at 6 cm, which is in close correspondence with the analytical estimates according to Bejan, 1982.

It may be noted that the Kelvin-Helmholtz waves become manifest at the perimeter of the jet/thermocline collision area. Indeed, from simultaneous temperature and velocity measurements, the centreline gradient Richardson number can be computed defined by :

$$Ri_g = -\frac{g}{\rho}\frac{d\rho}{dz}\left(\frac{du}{dz}\right)^{-2} \qquad (2)$$

It shows that on the centreline the gradient Richardson number exceeds the value of $^1/_4$ which is the classical criterion for shear layer instability.
Figure 4 shows long term (1 minute) averaged contour plots of the velocity and vorticity magnitude obtained by PTV and 2-dimensional direct numerical simulation (2D-DNS).

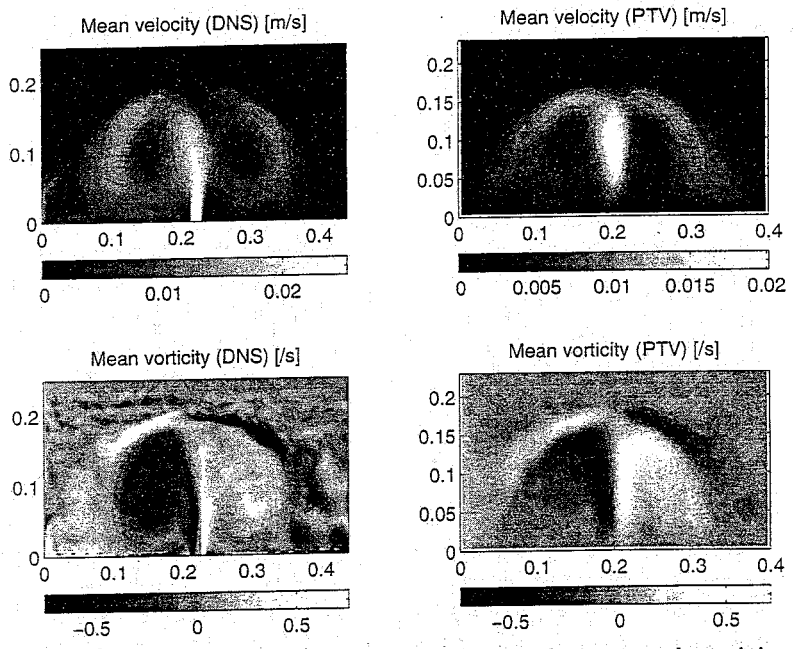

Figure 4 *1 minute averaged velocity magnitude (top) and vorticity (bottom) in grey scale, derived from PTV (right) and 2D-DNS (left). In the vorticity plots solid- and dashed lines represent contours with negative and positive values respectively.*

A clear difference appears at the jet origin where the matching of particles due to the relatively high velocity is poor. Another clear difference is the

considerably higher detail of the numerical simulation. It must be emphasised that typically 500 particles are matched in the PTV-routine, resulting in an average distance between particles of about 1.6 cm, which is considerably larger than the numerical grid spacing of 0.25 cm. As a result the spatial detection limit for vorticity (given an order of magnitude for velocity of 1 cms^{-1}) amounts to 0.6 s^{-1}, whereas it is 4 s^{-1} for the numerical simulation. Nevertheless, it is concluded that the overall pictures show strong similarities. To enhance the spatial resolution of the PTV, video recording is zoomed in on the shear layer area.

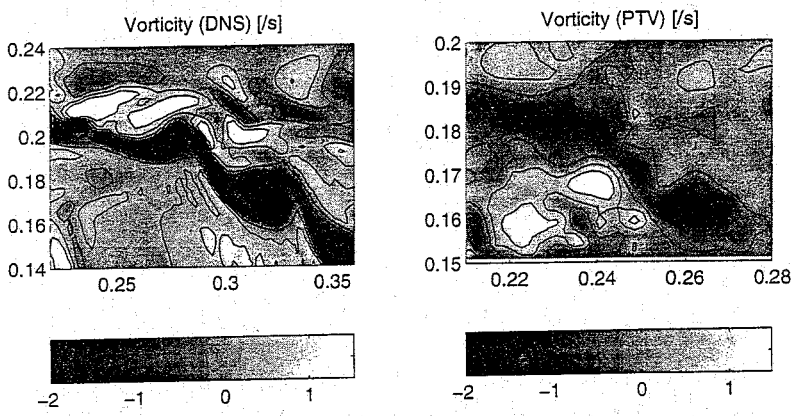

Figure 5 In grey scale vorticity derived by 2D-DNS (left) and PTV (right). For comparison only the range from -2 to +1.5 s^{-1} is shown, the DNS-results actually ranges from -6.1 to +2.5 s-1.

Due to the increased spatial resolution (average inter particle distance 0.3 cm) the vorticity distribution obtained by PTV agrees better with the 0.25 cm resolution DNS. Though the Kelvin-Helmholtz wave structure of this example shows close resemblance (showing an initial typical wave length of 5 cm), the DNS-result represents a case of stronger shear (higher vorticity) than the PTV-result. Indeed the propagation speeds of the main KH-node are found to be 1.2- (2D-DNS) and 0.6 (PTV) cms^{-1}.
To obtain insight in the 3D-effects of the flow field, PTV-measurements are done in planes perpendicular to the planes shown in the previous figures. Figure 6 gives a streaklines picture in the symmetry plane.

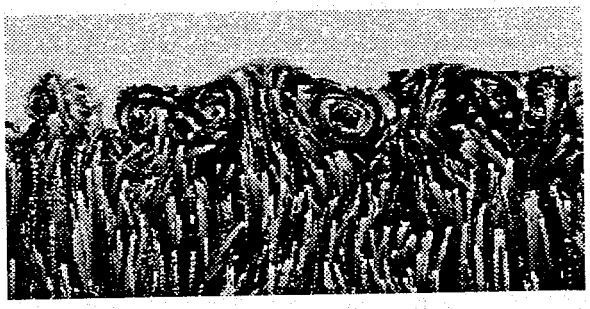

Figure 6 Side view video snapshot showing particle streaks in the symmetry plane. Window 20 x 10 cm^2. The white top part is the stagnant layer. Vertical undisturbed velocity ≈ 0.02 ms^{-1}.

Figure 6 shows the presence of vortices in the jet/thermocline collision area. The vortices most likely are Görtler vortices resulting from an unstable centrifugal flow field in the jet deflection area (higher centrifugal acceleration at smaller radius). As they superimpose an additional flow pattern on the primary jet- and the secondary Kelvin-Helmholtz flow they are depicted as tertiary. The length scale of the waves is estimated at $O(10^{-2})$ m. As the Görtler waves are driven by jet flow deflection, forcing takes place only in the jet stagnation region.
The Görtler waves occasionally entrain small amounts of fluid (cusps) from the thermocline. However, 2D-numerical simulation (excluding the Görtler vortices) agrees well with experiments with respect to entrainment rate and temperature frequency spectrum (Van Berkel, 1995), thereby also indicating that the effect of the tertiary Görtler vortices on the jet/thermocline interaction seems negligible. It appears that though the down-stream interaction between the primary- secondary and tertiary flow results in a quite complex flow field, the shear layer draw-down process is quite straight forward. Further analysis is required to confirm this premise.

4. ENTRAINMENT MECHANISM

The high resolution kinematic and thermodynamic insight provided by the numerical simulation enables detailed analysis of the entrainment process. Figure 7 provides the numerically obtained temperature distribution and entropy production rate corresponding with figure 5. The entropy production hereby serves to quantify the irreversible heat transfer rate in the storage. Unlike classical energy efficiencies, entropy based efficiency ac-

counts for internal heat transfer. The entropy production rate is given by eq. (3) :

$$s_{prod} = \lambda \left(\frac{|\nabla T|}{T} \right)^2 \qquad (3)$$

Eq. (3) accounts for entropy production due to diffusion of thermal energy only. It can be shown that entropy production due to viscous dissipation of mechanical energy is orders of magnitude lower[1].

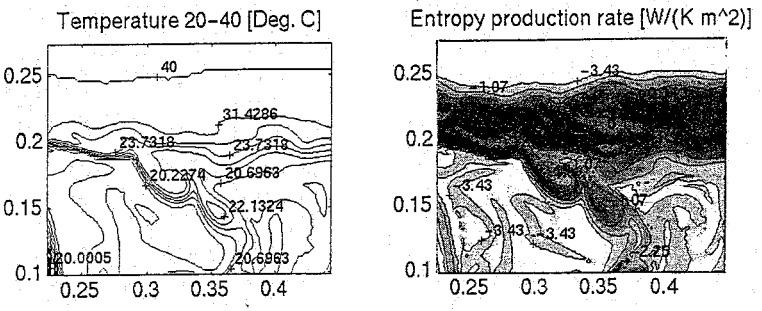

Figure 7 Isotherms and a ^{10}log grey scale plot of the local entropy production rate (per meter tank depth).

Clearly shown is how thermal energy is advected with the shear layer into the lower layer. Due to stretching and folding of the shear layer, the heat exchanging area of fluid particles increases while the normal width decreases. As a result diffusion of thermal energy is enhanced which causes the actual mixing of thermal energy. Figure 7 (right) shows that entropy is mainly produced in the thermocline which however is kept sharp due to the entrainment process. No entropy is produced in the upper stagnant layer. Visible in the lower layer are shear layer striations which have been chaotically mixed but still diffuse thermal energy.
The instantaneous entropy production rate in the entire domain (of which figure 6 is a sub-section) amounts to 39 10^{-3} W/K per meter tank depth. This instantaneous value should be compared with the time averaged value based on the amount of heat passing through the thermocline from the 40 °C to the 20 °C temperature reservoir. For this case the thermocline

1 The entropy production rate due to viscous dissipation at the most equals the jet kinetic energy (113 mW per meter tank depth) dissipated at a temperature of ≈ 300 K, yielding 0.38 10^{-3} W/K. Numerical evaluation on basis of the mechanical energy dissipation term confirmed this notion.

propagation speed has been determined at 10 μms^{-1}, corresponding with a heat flow of 371 W and a an average entropy production rate of 89 mW/K. Whether this mismatch is caused by time fluctuations or remaining numerical diffusion remains to be investigated.
Future investigations will comprise the entropy production analysis of real tanks, thereby providing the exergy based efficiency of application of a particular storage tank in an energy system.

5. CONCLUSIONS

1) Thermocline entrainment is caused by shear layers which detach during rebounding of colliding jet fluid.
2) Stretching and folding of the shear layer enhances diffusion of thermal energy which causes the actual mixing. Chaotic mixing in the lower layer blocks thermal energy return flow.
3) The non-buoyant jet is unstable and buckles with a typical wave length of 6 cm and a frequency of $\approx 1/3$ Hz. The shear layers are unstable to Kelvin-Helmholtz waves with typical wave length of 5 cm and a frequency of $1/3$ Hz. In the jet collision area Görtler vortices develop, occasionally entraining small cusps of fluid into the lower layer. Their effect on the local entrainment mechanism however is negligible.
4) Most of the entropy is produced in the thermocline.

Future work will comprise application of the 2D-DNS code to real stores and 3D-DNS of the vertical jet experiment. Finally the storage geometry will be optimized with respect to thermocline entrainment and thermocline thickness.

REFERENCES

Bastiaans RJM, Van Steenhoven AA, Rindt CCM, Nieuwstadt FTM (1994) Direct and Large–Eddy Simulation of Transient Buoyant Plumes : A Comparison with an Experiment. In : Voke, PR and JP Chollet (eds) *Direct and Large-Eddy Simulation I. Selected papers from the first ERCOFTAC workschop on Direct and Large-Eddy Simulation*, Kluwer Academic Publishers pp 399-410.

Bejan A 1982 *Entropy generation through heat and fluid flow* ISBN 0-471-09438-2 A Wiley-Interscience publication.

Dalziel S (1995) *DigImage Image processing for fluid dynamics*. Cambridge Environmental Research Consultants. Cambridge.

Harlow FH, Welch JE (1965) Numerical Calculation of Time-Dependent Viscous Incompressible Flow of Fluid with Free Surface, *The Physics of Fluids 8(12)* : 2182-2189.

Hussain M A, Wildin MW (1991) Studies on mixing on the inletside of the thermocline in diurnal stratified storage. In : Snijders AL, *Proceedings of the 5th Int. conference on thermal energy storage Thermastock '91*, May 13-16, Scheveningen, The Netherlands, pp 8.5_1-8.5_7

Schumann U, Sweet R (1976) A direct method for the solution of Poisson's equation with Neumann boundary conditions on a staggered grid of arbitrary size. *J of Computational Physics* 20 : 171 – 182, 1976.

Van Berkel J (1995) Mixing in Short Term Thermal Stratified Energy Storage, presented at the 1995 Solar World Congress "In Search of the Sun", Harare, Zimbabwe, September 1995.